Satellite Investigation of the M_2 Internal Tide in the Tasman Sea

ZHONGXIANG ZHAO

Applied Physics Laboratory, University of Washington, Seattle, Washington

MATTHEW H. ALFORD

Scripps Institution of Oceanography, University of California, San Diego, La Jolla, California

HARPER L. SIMMONS AND DMITRY BRAZHNIKOV

College of Fisheries and Ocean Sciences, University of Alaska Fairbanks, Fairbanks, Alaska

ROB PINKEL

Scripps Institution of Oceanography, University of California, San Diego, La Jolla, California

(Manuscript received 9 March 2017, in final form 11 January 2018)

ABSTRACT

The M_2 internal tide in the Tasman Sea is investigated using sea surface height measurements made by multiple altimeter missions from 1992 to 2012. Internal tidal waves are extracted by two-dimensional plane wave fits in 180 km by 180 km windows. The results show that the Macquarie Ridge radiates three internal tidal beams into the Tasman Sea. The northern and southern beams propagate respectively into the East Australian Current and the Antarctic Circumpolar Current and become undetectable to satellite altimetry. The central beam propagates across the Tasman Sea, impinges on the Tasmanian continental slope, and partially reflects. The observed propagation speeds agree well with theoretical values determined from climatological ocean stratification. Both the northern and central beams refract about 15° toward the equator because of the beta effect. Following a concave submarine ridge in the source region, the central beam first converges around 45.5°S, 155.5°E and then diverges beyond the focal region. The satellite results reveal two reflected internal tidal beams off the Tasmanian slope, consistent with previous numerical simulations and glider measurements. The total energy flux from the Macquarie Ridge into the Tasman Sea is about 2.2 GW, of which about half is contributed by the central beam. The central beam loses little energy in its first 1000-km propagation, for which the likely reasons include flat bottom topography and weak mesoscale eddies.

1. Introduction

Theoretical and numerical studies have long identified the Macquarie Ridge to be a site of strong barotropic-to-baroclinic tidal conversion (e.g., Morozov 1995; Niwa and Hibiya 2001). Outgoing internal tides from the Macquarie Ridge have been simulated using global high-resolution internal tide models (Simmons et al. 2004; Arbic et al. 2010). Simmons et al. (2004) found that the Macquarie Ridge radiates energetic M_2 internal tides into the Tasman Sea and that one well-defined internal tidal beam propagates across the Tasman Sea and impinges on the Tasmanian continental slope (see their Fig. 8). In Hybrid Coordinate Ocean Model (HYCOM) runs that simulate internal tide, eddy, and ocean circulation simultaneously, Arbic et al. (2010) found that the transbasin internal tidal beam reaches the Tasmanian slope even in the presence of large-scale circulation and mesoscale eddies (see their Fig. 4). The transbasin internal tidal beam from the Macquarie Ridge has been observed by satellite altimetry (Ray and Zaron 2016; Zhao et al. 2016), supporting previous numerical simulations. The satellite altimetric results imply that the M_2 internal tide is phase locked (at least partially) with the barotropic tidal forcing over a 20-yr period. Both the satellite and modeled results reveal that the transbasin beam loses little energy in its first ≈1000 km propagation. On the Tasmanian slope, the incoming internal tide may reflect back into the Tasman

Corresponding author: Zhongxiang Zhao, zzhao@apl.washington.edu

DOI: 10.1175/JPO-D-17-0047.1

© 2018 American Meteorological Society. For information regarding reuse of this content and general copyright information, consult the AMS Copyright Policy (www.ametsoc.org/PUBSReuseLicenses).

Sea (Johnston et al. 2015; Klymak et al. 2016). The central Tasman Sea is relatively quiescent; however, its southern and northwestern parts are affected by the Antarctic Circumpolar Current (ACC) and the East Australian Current (EAC), respectively (Chiswell et al. 2015). The Tasman Sea thus provides an ideal site to investigate the propagation, reflection, and dissipation of internal tides, thanks to its complex dynamic environment and long-range internal tide propagation (Fig. 1).

The Tasman Tidal Dissipation Experiment (TTIDE) was motivated to study the shoaling internal tide on the Tasmanian continental slope (Pinkel et al. 2015). It was complemented by two accompanying projects: T-Beam and T-Shelf. T-Beam was designed to quantify the incoming internal tide in the open ocean (Waterhouse et al. 2018, manuscript submitted to *J. Phys. Oceanogr.*). T-Shelf was designed to study the nonlinear evolution on the shallower Tasmanian continental shelf (Pinkel et al. 2015). The combined TTIDE/T-Beam/T-Shelf experiment tracked the transbasin beam from its generation on the Macquarie Ridge to propagation in the Tasman Sea and evolution on the Tasmanian slope. The field experiment was conducted from January to March 2015, in which internal tides were sampled using a variety of instruments including moorings, shipboard CTD–LADCP, fastCTD, and gliders (Johnston et al. 2015; Pinkel et al. 2015). The field experiment was supported with numerical modeling (e.g., Klymak et al. 2016) and satellite altimetry.

Results from the TTIDE/T-Beam/T-Shelf experiment have potential global implications. First, the global barotropic tide loses energy to internal tides at a rate of 1 TW, and a significant fraction is transported away by low-mode internal tides (Egbert and Ray 2000; Alford 2003; Alford et al. 2007). The breaking of internal tides induces diapycnal mixing, which plays an important role in maintaining ocean stratification and meridional overturning circulation (MOC; Munk and Wunsch 1998; Wunsch and Ferrari 2004; Kunze 2017a,b). The MOC is sensitive to the magnitude and geography of ocean mixing (Melet et al. 2013, 2016). An important scientific question is where and how the outgoing internal tide eventually dissipates (Alford and Zhao 2007; MacKinnon et al. 2013, 2017). Second, a fraction of low-mode internal tides travels across the ocean basins and impinges on the opposite continental slopes (Kelly et al. 2013; Waterhouse et al. 2014; Buijsman et al. 2016); however, the dynamic processes caused by the incoming internal tides remain poorly understood. Previous studies have revealed that the incoming internal tides may scatter into high-mode internal waves, induce lee waves and internal solitary waves, and reflect back into the open ocean (e.g., Johnston and Merrifield 2003; Nash et al. 2004; Helfrich and Grimshaw 2008; Legg and Klymak 2008; Klymak et al. 2011; Kelly et al. 2012, 2013; Martini et al. 2013). Additionally, the incoming internal tides may modulate the local generation of internal tides (Kerry et al. 2013; Ponte and Cornuelle 2013; Buijsman et al. 2014). Ocean mixing on the continental slope is believed to contribute significantly to the global diapycnal mixing budget (Kunze et al. 2006, 2012; Pinkel et al. 2015; Waterhouse et al. 2017). The TTIDE/T-Shelf/T-Beam field experiment is motivated to improve our understanding of these dynamic processes.

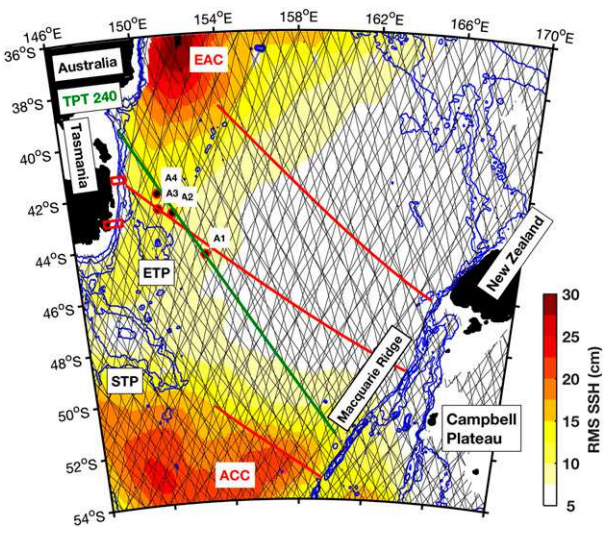

FIG. 1. The Tasman Sea. ETP and STP stand for east Tasman Plateau and south Tasman Plateau, respectively. EAC and ACC stand for the East Australian Current and the Antarctic Circumpolar Current, respectively. Blue lines indicate bathymetric contours of 1000-, 2000-, and 3000-m depth. Black lines indicate ground tracks of multiple satellite altimeter missions. The satellite track TPT 240 is shown in green. Red lines indicate three M_2 internal tidal beams originating on the Macquarie Ridge. Red boxes indicate two TTIDE survey paths on the Tasmanian continental slope. Red circle A1 indicates the T-Beam offshore mooring. Red circles A2, A3, and A4 indicate a TTIDE antenna array deployed to determine the reflected internal tide. Color shading denotes the RMS (root mean square) SSH, which is a proxy of the background eddy kinetic energy (EKE) field.

In this paper, we will address the following question: What is the spatial distribution of the M_2 internal tide in the Tasman Sea? Satellite altimetry measures internal tides via their centimeter-scale sea surface height (SSH) fluctuations (Ray and Mitchum 1996). The main advantage of satellite altimetry is its near-global view of the internal tide field from space (Ray and Cartwright 2001; Zhao and Alford 2009). Recent advances in mapping internal tides by satellite altimetry are mainly due to the accumulation of multiyear multisatellite altimeter data since 1992. Multisatellite altimetry has denser ground tracks than any single mission and better

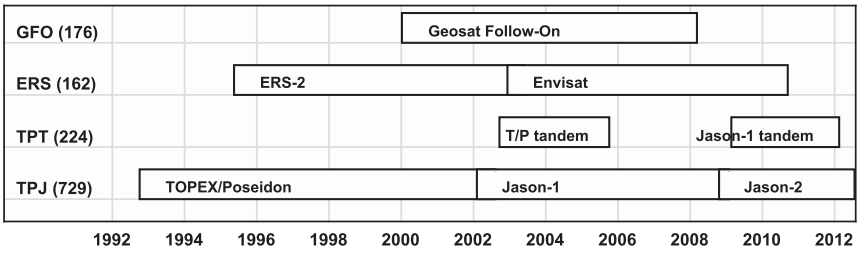

FIG. 2. The temporal coverage of four sets of satellite altimeter data during 1992–2012. For each dataset, the number in brackets gives the record length or the number of repeat cycles.

resolves the relatively small-scale (mode-1 M_2 wavelength ranges of 120–200 km) internal tides (Zhao et al. 2011; Ray and Zaron 2016). The present paper focuses on the M_2 internal tide in the Tasman Sea. We will extract the M_2 internal tide using an improved plane wave fit method, which is able to resolve multiwave interference (Zhao and Alford 2009). For the first time, we observe three incident and two reflected internal tidal beams in the Tasman Sea originating from the Macquarie Ridge. The separately resolved internal tidal waves enable us to investigate the internal tide's refraction, convergence, divergence, and reflection, none of which has been observed in this region by satellite altimetry. Our satellite altimetric results may provide a spatial context for better interpreting the TTIDE/T-Beam/T-Shelf field measurements.

This paper is arranged as follows: In section 2, we will describe the satellite altimeter data used in this study and our improved mapping technique. In section 3, we will present the M_2 internal tide field in the Tasman Sea, with a focus on the transbasin internal tidal beam. Section 4 gives a summary.

2. Data and methods

a. Satellite altimeter data

The satellite altimetric SSH data used in this study are from multiple missions including TOPEX/Poseidon (TP), *Jason-1* (J1), *Jason-2* (J2), *ERS-2*, *Environmental Satellite* (*Envisat*), and *Geosat Follow-On* (*GFO*). They are along four sets of predetermined ground tracks, which we refer to as TPJ, TPT (TP tandem), ERS, and GFO, respectively (Fig. 2). The SSH data products have been processed by applying standard corrections for atmospheric effects, surface wave bias, and geophysical effects. The barotropic tide and loading tide are corrected using Global Ocean Tide 4.7 (GOT4.7; AVISO 2012). All SSH measurements in waters shallower than 500 m are discarded. The along-track gridded data are produced by Ssalto/Duacs and distributed by the French AVISO data center. The satellite SSH products were downloaded on 18 January 2013. The satellite altimeter data since 2013 are currently available but not used in this paper. The same datasets have been used to construct the global mode-1 M_2 and S_2 internal tide fields (Zhao et al. 2016; Zhao 2017).

These datasets have different temporal coverage. For each dataset, the record length (i.e., the number of repeat cycles) is given in Fig. 2. Among them, TPJ has the longest time series from 1992 to 2012, consisting of data from TP, J1, and J2. Harmonic analysis has been widely used to extract tidal signals by the least squares fit. According to the Rayleigh criterion, all four datasets are long enough to reliably separate the M_2 internal tide from other major tidal constituents such as S_2 and K_1 (Zhao et al. 2011; Ray and Zaron 2016). However, the repeat periods of TPJ (TPT), ERS, and GFO are 10, 35, and 17 days, respectively. As a result of these long repeat cycles, the high-frequency M_2 signal aliases to longer periods, which overlap with the wide spectrum of mesoscale eddies. Therefore, the harmonically fitted internal tides are severely contaminated by nontidal signals leaked from mesoscale eddies (Ray and Zaron 2016; Zhao et al. 2016).

b. Two-dimensional plane wave fit

A two-dimensional plane wave fit method is employed to extract internal tidal waves. This method is a variant of harmonic analysis (Ray and Cartwright 2001; Zhao et al. 2011). It extracts internal tides (on track or off track) using SSH measurements in a fitting window (180 km by 180 km in this study), which contains a space–time record of 7–11 $\times$ 10^4 SSH measurements (a function of latitude), combining multiple altimeter missions over 20 years. This method can significantly suppress nontidal noise (Zhao et al. 2016). Following an iterative procedure, we can extract multiple internal tidal waves one by one and separate them according to propagation direction. The separately resolved fields enable us to investigate the incident and reflected internal tides in the Tasman Sea. We refer the interested

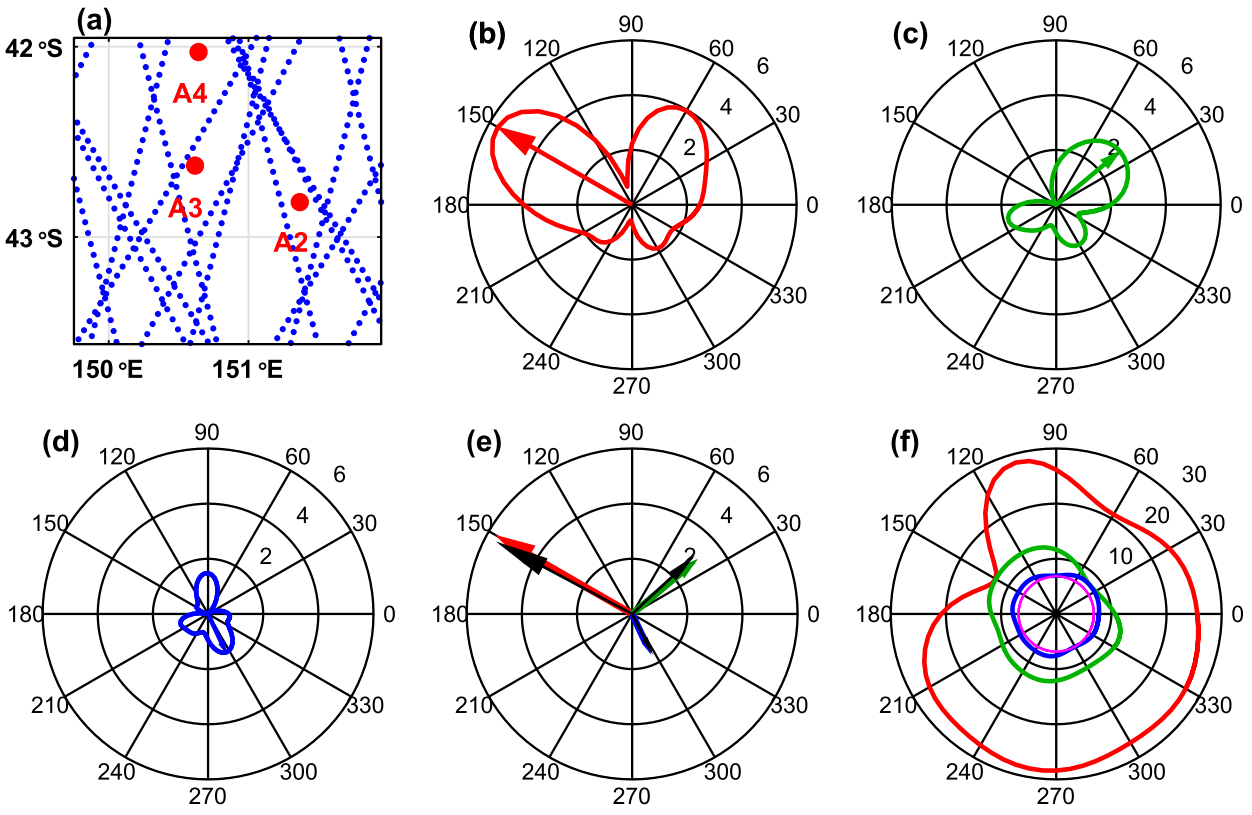

FIG. 3. An example of the two-dimensional plane wave fit method. Three mode-1 M_2 internal tidal waves are extracted. (a) Positions of SSH data in a 180 km by 180 km fitting window, which is selected here to cover three TTIDE moorings A2–A4 (red dots). (b) Amplitude (mm) vs direction obtained by fitting a plane wave in each compass direction. The first internal tidal wave (red arrow) is determined from the largest lobe. (c) After removing the predicted signal of the first wave from the SSH data, this procedure is repeated to determine the second wave (green arrow). (d) As in (c), but to determine the third wave (blue arrow). (e) Each wave is refitted with the other two waves temporarily removed. Black arrows show the finally determined internal tidal waves. (f) Residual variance (mm^2) associated with the plane wave fitting. The final residual variance (inner pink circle) is almost isotropic.

reader to Zhao et al. (2016) for a detailed description of this method.

An example is given in Fig. 3 to demonstrate how to extract M_2 internal tidal waves at an off-track point. This region is selected to cover three TTIDE moorings A2–A4 (Fig. 3a). The procedure is as follows: First, in each compass direction (angular increment is 1°), the amplitude and phase of one plane wave are determined by the least squares fit. When the resultant amplitudes are plotted as a function of direction in polar coordinates, an internal tidal wave appears to be a lobe (Fig. 3b). The amplitude, phase, and direction of the first M_2 wave are determined from the biggest lobe (red arrow). We then predict the SSH signal of the above determined wave and remove it from the original SSH data. This step removes not only the wave itself but also its sidelobes, which are caused by irregular spatial distribution of ground tracks (Zhao et al. 2011). This procedure can be repeated to extract an arbitrary number of waves. Here, we repeat it two more times to extract three M_2 internal tidal waves in total. After extracting three waves, the residual variance is almost equal for all directions. Finally, each wave is refitted with the other two waves temporarily removed in order to reduce the cross-wave interference. Figure 3f shows the residual variance versus direction in each step, indicating that the internal tidal waves can also be determined by minimal residual variance.

c. *Improvements over Zhao et al. (2016)*

Previous studies usually employed an along-track high-pass filter with a cutoff wavelength of 500 km to remove barotropic tidal residual and long-wavelength nontidal noise (Ray and Zaron 2016; Zhao et al. 2016). Such a high-pass filter has proven efficient in suppressing background noise and significantly improved the internal tide mapping. However, high-pass filtering is problematic in the Tasman Sea. The M_2 internal tide in this region propagates dominantly toward northwest. It is generally parallel to the northwestward satellite tracks

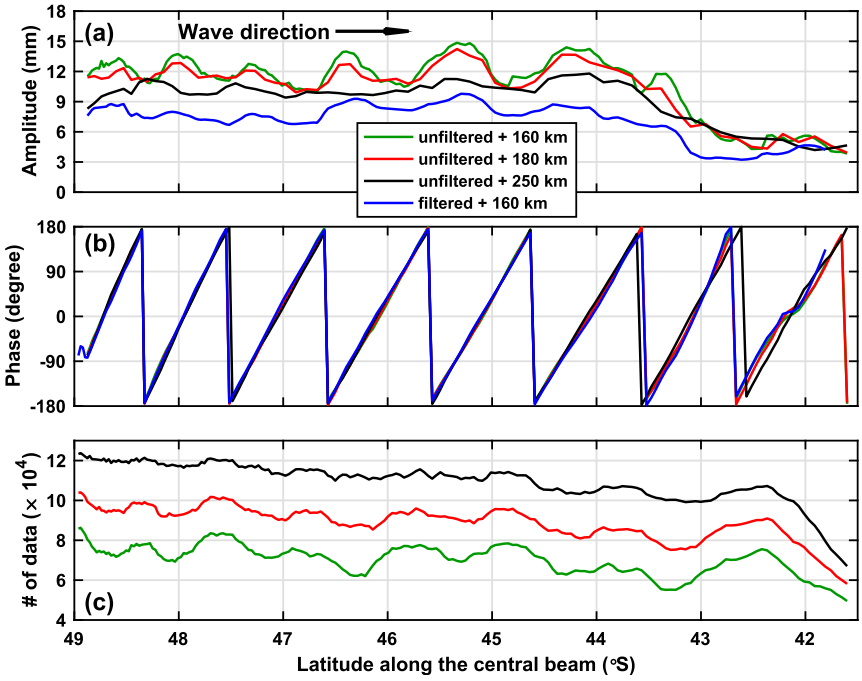

FIG. 4. (a) Amplitude and (b) phase of the M_2 internal tide along the transbasin central beam in the Tasman Sea. See beam location in Fig. 1. The green, red, and black lines denote the M_2 internal tides obtained using the unfiltered data and fitting windows of 160 km by 160 km, 180 km by 180 km, and 250 km by 250 km, respectively. The blue lines denote those obtained using the filtered data and 160 km by 160 km windows. The comparison suggests that the M_2 internal tide was previously underestimated by along-track filtering. (c) Number of SSH data per fitting window. Its spatial variation leads to the wiggles on the resultant M_2 amplitude.

but perpendicular to the northeastward tracks (Fig. 1). Along the northeastward tracks, the projected M_2 internal tide has a wavelength much longer than 500 km. As a result, the along-track, high-pass filter removes the internal tide signal and underestimates the M_2 amplitude.

To address this issue, we here extract the M_2 internal tide using the unfiltered SSH data. As noticed in previous studies, the unfiltered SSH data contain substantial nontidal noise. To suppress noise, we fit plane waves in 180 km by 180 km windows instead of the 160 km by 160 km windows used in Zhao et al. (2016). With larger fitting windows, we have more independent SSH data and better suppress nontidal noise. The 180-km window is selected also because it is close to one wavelength of the M_2 internal tide in the Tasman Sea. As shown in Fig. 3, M_2 internal tidal waves can be unambiguously determined using the unfiltered SSH data and a 180 km by 180 km fitting window.

Our improvements are illustrated in Fig. 4 by comparing the M_2 internal tides obtained using the filtered and unfiltered SSH data. This example is along the transbasin internal tidal beam in the Tasman Sea (Fig. 1, red curves). The blue line in Fig. 4a denotes the M_2 amplitudes obtained using the filtered data and 160 km by 160 km windows. For comparison, the green line denotes those using the unfiltered data and 160 km by 160 km windows. The latter are much greater than the former, suggesting that the M_2 amplitudes, which were previously underestimated, are now improved using the unfiltered data (Fig. 4a). The red line denotes the M_2 amplitudes obtained using the unfiltered data and 180 km by 180 km windows (used in this study). The amplitudes are slightly lower and smoother than those using 160 km by 160 km windows because of larger fitting windows. Figure 4b shows that the resultant phases using the filtered and unfiltered data agree with each other very well, with their differences mostly less than 15°. The wiggles on the amplitudes are due to the irregular distribution of altimeter data and thus different numbers of SSH per fitting window. As shown in Fig. 4c, for both the 160- and 180-km windows, there are spatial variations on the number of SSH data per fitting window, consistent with their spatial variations on the resultant amplitude. To further support this point, we show the M_2 amplitudes obtained using the unfiltered data and 250 km by 250 km windows (Fig. 4a, black). The

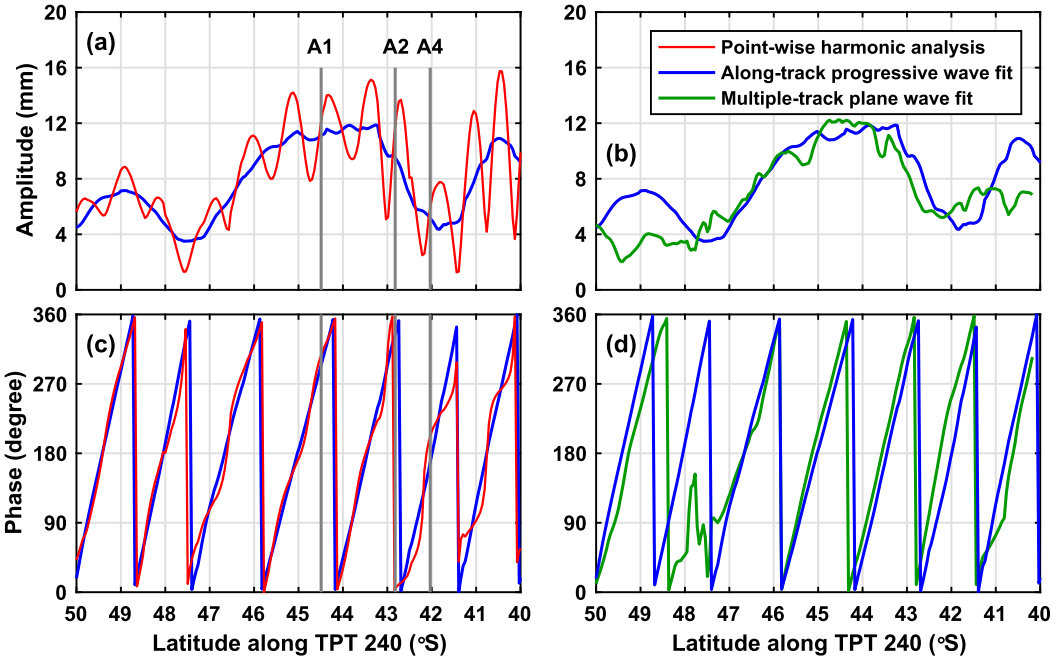

FIG. 5. Comparisons of the M_2 internal tides along TPT 240 obtained using different methods: pointwise harmonic analysis, along-track progressive wave fit, and multitrack plane wave fit. (a) Amplitude and (c) phase of the M_2 internal tides from harmonic analysis (red) and progressive wave (blue) fit. The vertical lines mark three moorings A1, A2, and A4. See their locations in Fig. 1. (b) Amplitude and (d) phase of the M_2 internal tides from the progressive wave and plane wave (green) fits.

number of SSH data per window does not fluctuate much (Fig. 4c); therefore, the resultant M_2 amplitudes are much smoother. However, our above analysis cannot exclude the possibility that the wiggles may be caused by multiwave interference (Zhao and Alford 2009; Rainville et al. 2010). The sparse satellite tracks preclude us from examining this phenomenon.

d. Comparisons of 1D and 2D results

In this section, we compare the M_2 internal tides extracted by multitrack plane wave fits (2D) and single-track progressive wave fits (1D). The former is conducted using SSH data in 180 km by 180 km windows. The latter uses SSH data in 180-km sections along individual tracks. Therefore, the 1D and 2D results are from different fitting windows. This analysis is motivated by a concern that our 180 km by 180 km fitting windows might lead to underestimation of the M_2 amplitude. Along-track progressive wave fit is another variant of harmonic analysis (Zhao and Alford 2009). Similar to plane wave fitting using multiple tracks, this technique extracts internal waves along one single track. We can extract two progressive waves in opposite directions along one track. The fitting is conducted in sliding 180-km sections along one track, in the same manner as plane wave fits.

Figure 5 shows the M_2 internal tides along TPT 240 using three different methods: pointwise harmonic analysis (red), along-track progressive wave fit (blue), and multitrack plane wave fit (green). The harmonically fitted result contains the multiwave superimposition and thus half-wavelength wiggles because it cannot resolve multiwave interference. For the along-track and multitrack results, we keep the dominant northwestward component only. We find that the results agree well, both in amplitude and phase (Figs. 5b,d). TPT 240 is selected because it overlaps with three field moorings A1, A2, and A4 (Fig. 5a). A detailed comparison between the altimetric and moored observations will be reported separately.

We further compare the along-track and multitrack results for all northwestward tracks in the Tasman Sea. The four panels are for TPJ, TPT, ERS, and GFO, respectively (Fig. 6). The GFO comparison is an exception because the M_2 signal in the GFO data aliases to 317 days, close to the annual cycle (Ray et al. 2011; Zhao et al. 2011). The GFO observed M_2 internal tides are contaminated by the annual cycle and too noisy to draw any conclusion. For TPJ, TPT, and ERS, we find that the multitrack and along-track results agree very well. For each dataset, the multitrack and along-track resultant variances are close. The RMS differences are 1.3, 2.3, and 2.6 mm for TPJ, TPT, and ERS, respectively. We

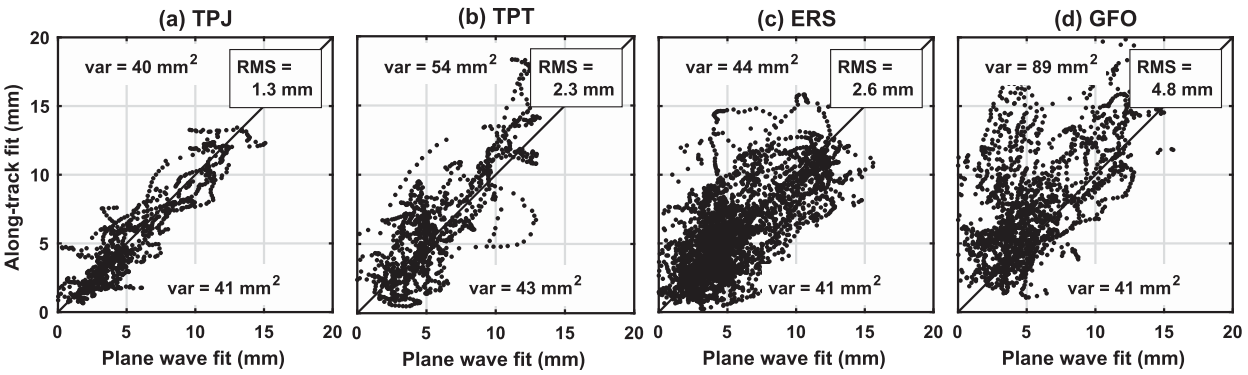

FIG. 6. Comparisons of the M_2 amplitudes obtained by the multitrack plane wave fit and along-track progressive wave fit methods. The comparisons are for the northwestward ground tracks only. See their locations in Fig. 1. The four panels are for four SSH datasets: (a) TPJ, (b) TPT, (c) ERS, and (d) GFO. For each panel, the SSH variances and their RMS differences are given.

thus draw the conclusion that our plane wave fits in 180 km by 180 km windows do not significantly underestimate the M_2 internal tide.

3. Results

a. Regional mapping in the Tasman Sea

We construct the M_2 internal tide field in the Tasman Sea by fitting plane waves as described in section 2. Our mapping region ranges from 56° to 36°S, 145° to 170°E. The fitting is conducted at a regular grid of 0.1° longitude by 0.1° latitude. At each grid point, three M_2 internal waves are extracted in a fitting window of 180 km by 180 km (Fig. 3). The large window and small grid imply that neighboring fitting windows are mostly overlapped. Figure 7 shows two snapshot SSH fields of the resultant M_2 internal tide. The internal tide solution may be contaminated by energetic mesoscale eddies in the EAC and ACC regions. In Fig. 7, dots are used to mask regions with the RMS SSH greater than 10 cm. In addition, the internal tide solution in waters shallower than 2000 m is discarded, which does not affect our internal tide observations in the deep region.

Figure 7a shows the three-wave superimposed SSH field. It shows clearly the dominant transbasin internal tidal beam in the Tasman Sea and southeastward internal tidal beams to the east of the Macquarie Ridge. Because of multiwave interference, however, it is difficult to detect individual beams. Figure 7b shows the dominant northwestward internal tide component only. This component is extracted from the three-wave solution based on propagation direction. At each grid point, we keep the waves with propagation direction ranging 90°–200° counterclockwise from due east.

The dynamics of internal tides have long been studied (Munk et al. 1965; Wunsch 1975; Gill 1982). Theoretical relations between their sea surface and interior properties have been established (Kunze et al. 2002; Wunsch 2013). Recent studies have derived the conversion relation (a function of location) from the SSH amplitude to the depth-integrated energy flux (Zhao et al. 2016). Accordingly, the depth-integrated energy flux is calculated from the fitted SSH amplitude. To avoid repetition, we refer the interested reader to Zhao et al. (2016) for a detailed description of the calculation procedure (their appendix A). Figure 7c shows flux vectors of all three waves at each grid point, while Fig. 7d shows the total flux of the northwestward component. In the remainder of this section, we will investigate these long-range internal tidal beams propagating toward northwest. In section 3f, we will extract the northeastward component to investigate reflected internal tides off the Tasmanian slope.

b. Three internal tidal beams

The internal tide radiation from the ≈1300-km-long Macquarie Ridge is spatially inhomogeneous (Fig. 7b), similar to the Hawaiian Ridge (Merrifield et al. 2001; Carter et al. 2008). The barotropic-to-baroclinic tidal conversion is mainly determined by ocean stratification, tidal current, and bottom topography (Garrett and Kunze 2007). In this region, the generation is likely also affected by the multisource resonance between the Macquarie Ridge and the Campbell Plateau to the east (Fig. 1), similar to the two-ridge resonance in the Luzon Strait (Buijsman et al. 2014). The distance between the Macquarie Ridge and the Campbell Plateau ranges from tens of kilometers near New Zealand to about 400 km at 54°S. In the separately resolved field (Figs. 7b,d), one can see that the Macquarie Ridge radiates three M_2 internal tidal beams into the Tasman Sea. The three red lines in Figs. 1 and 7 delineate their central paths. Their basic properties are summarized in Table 1.

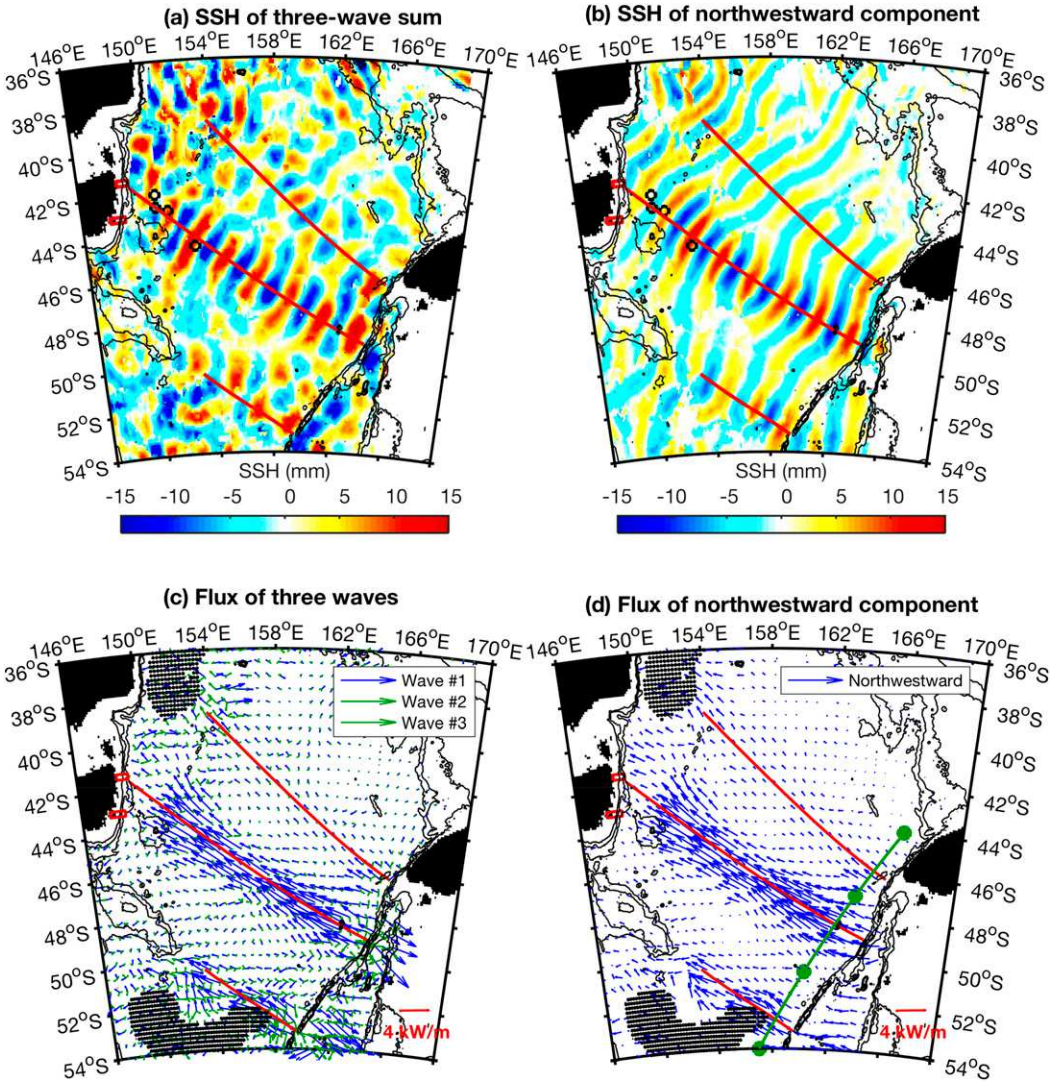

FIG. 7. The M_2 internal tide in the Tasman Sea. Snapshot SSH fields: (a) three-wave sum and (b) northwestward component only. Depth-integrated energy fluxes: (c) all three internal waves at each grid point are shown. For clarity, flux vectors are given at every sixth grid point. (d) As in (c), but for the northwestward internal waves only, with propagation direction ranging 90°–200°. The energy flux across the green line is integrated to be 2.2 GW. The energy fluxes are about 0.7, 1.1, and 0.4 GW for the southern, central and northern beams (bounds are marked by dots), respectively. In all panels, red lines indicate three internal tidal beams originating on the Macquarie Ridge. Black lines indicate bathymetric contours of 1000, 2000 and 3000 m depth. Dotted regions indicate the energetic EAC and ACC regions (RMS SSH >10 cm), where the internal tide solution may be contaminated by nontidal noise.

The northern beam originates in the region where the Macquarie Ridge meets the New Zealand continental slope. Compared to the central beam, the northern beam is much weaker and barely detected. We consult with the M_2 internal tide fields simulated using three numerical models: GOLD (Simmons et al. 2004), STORMTIDE (Müller 2013), and HYCOM (Savage et al. 2017). All three models suggest the existence of the weak northern beam. This beam propagates over 1200 km into the EAC extension region and becomes undetectable to satellite altimetry. Possible reasons for its disappearance include (i) loss of phase locking with the barotropic tidal forcing, (ii) dissipation in the EAC, and (iii) being masked by mesoscale eddies. A detailed investigation of their relative importance is beyond the scope of this paper.

The southern beam can be tracked for about 500 km by satellite altimetry. Note that its source also lies in the

TABLE 1. Information on three internal tidal beams in the Tasman Sea.

Beam	Source region	Initial direction (CCW from east)	Propagation distance (km)	Width (km)	Flux (GW)	Destination region
Northern	165.5°E, 46°S	≈145°	1240	400	0.4	EAC
Central	163.5°E, 49°S	≈160°	1540	420	1.1	EAC, slope
Southern	159.5°E, 53°S	≈140°	550	380	0.7	ACC

ACC region. It is expected that both the generation and propagation of this beam are strongly modulated by the ACC. It is a surprise that this beam can be detected by satellite altimetry, which means that at least a fraction of the M_2 internal tide is phase locked with the barotropic tidal forcing over a 20-yr period (Ray and Zaron 2011; Zaron 2017). Further diagnosis of its temporal variability, its effects on turbulence, and the influence of the ACC is not a goal of this paper (e.g., Waterman et al. 2013).

The central beam propagates over 1500 km and reaches the Tasmanian continental slope, consistent with previous numerical simulations (Simmons et al. 2004; Arbic et al. 2010). As shown in Fig. 1, the beam travels through a relatively quiescent ocean environment in its first ≈1000-km propagation. Before arriving at the Tasmanian slope, it encounters energetic eddies associated with the southern branch of the EAC. This transbasin beam is the target of the TTIDE/T-Shelf/T-Beam field experiment.

c. *Propagation speed*

We next examine the propagation speed of these three internal tidal beams and compare the observed speeds with theoretical values. In Fig. 8, the along-beam Greenwich phase is shown in the upper panels. The along-beam propagation speed, calculated from the along-beam phase gradient, is shown in the bottom panels (black lines).

Theoretical propagation speeds are calculated in two steps. First, the eigenvalue speeds C_n are obtained by solving the Sturm–Liouville equation (Gill 1982) using climatological ocean stratification profiles in the *World Ocean Atlas 2013* (Locarnini et al. 2013; Zweng et al.

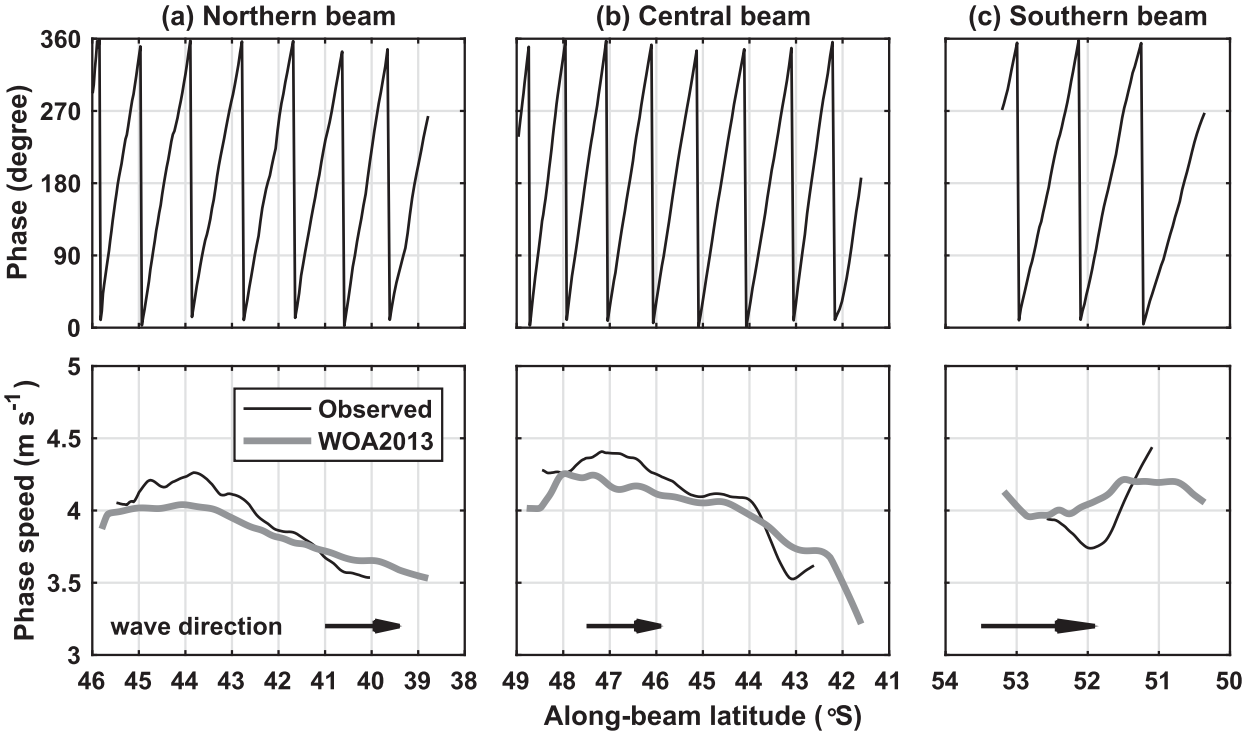

FIG. 8. Greenwich phase (top) and propagation speed (bottom) along three internal tidal beams. The observed speeds are derived from along-beam phase gradients. The theoretical speeds are calculated using climatological ocean stratification profiles in the World Ocean Atlas 2013 (WOA2013). The observed and theoretical speeds agree well.

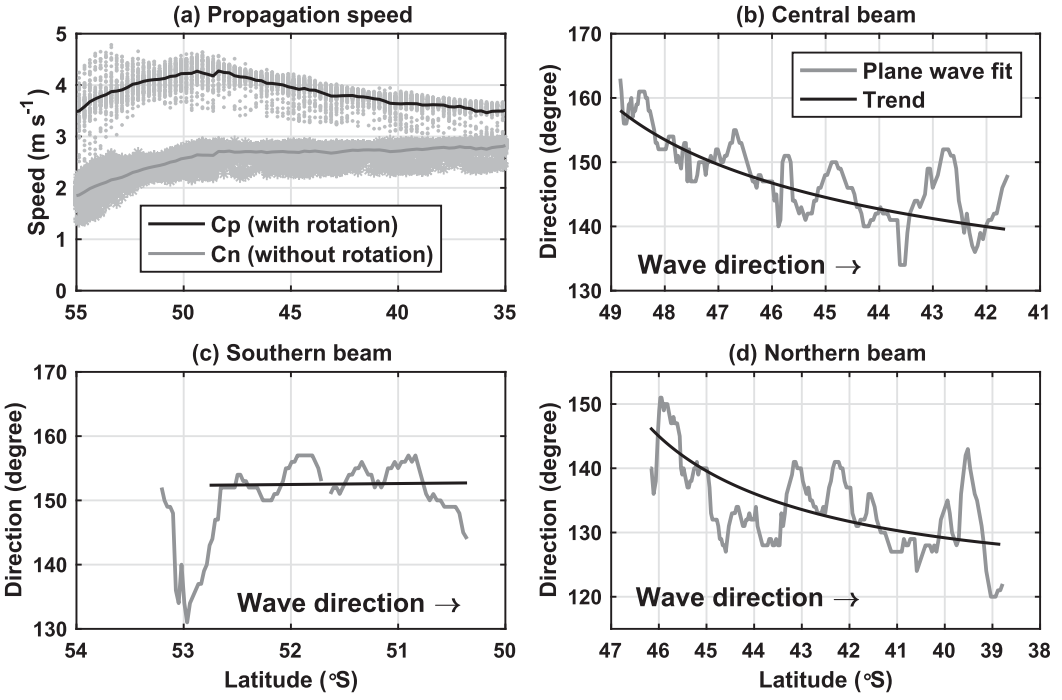

FIG. 9. Refraction of the M_2 internal tide because of the beta effect. (a) Propagation speeds in the Tasman Sea (depth > 3000 m only). Asterisks and dots denote the eigenvalue and phase speeds, respectively. Curves are their zonal means. (b) Propagation direction of the M_2 internal tide along the central beam. The gray line indicates the plan wave fitted result. The black line is the second-order polynomial fit. (c) As in (b), but for the southern beam. (d) As in (b), but for the northern beam. Both the northern and central beams refract about 15° toward the equator.

2013). Second, the phase C_p and group C_g speeds are, respectively, calculated following

$$C_p = \omega(\omega^2 - f^2)^{-1/2} C_n, \tag{1}$$

and

$$C_g = \omega^{-1} (\omega^2 - f^2)^{1/2} C_n, \tag{2}$$

where ω is the M_2 tidal frequency, and f is the locally inertial frequency (Rainville and Pinkel 2006). The C_n only varies with stratification and depth, while both C_p and C_g vary with latitude as well as stratification and depth. Because the Tasman Sea is at high latitudes, $|f|$ is close to the M_2 frequency (at 75°S, $|f| \approx \omega_{M2}$). Specifically, $|f|$ ranges from 1.2 to 1.5 cycles per day (cpd), close to 1.932 cpd for M_2. In the deep central Tasman Sea, C_p varies little with the weak spatial variation of depth and stratification (section 3d) but significantly with latitude. Figure 8 shows that the observed speeds agree with the theoretical values very well. For the northern and central beams, the observed speeds are generally larger than the theoretical speeds. The largest difference is about 0.2 m s^{-1} or 5% of the absolute speed. This discrepancy is understandable for the following reasons: 1) The observed speeds are derived from a 20-yr-long, phase-locked internal tide field from satellite altimetry. In contrast, the theoretical speeds are calculated from ocean stratification profiles constructed using all historical in situ measurements. 2) The theoretical speeds do not consider the effect of background currents and eddies.

d. Refraction caused by the β effect

In this section, we demonstrate that the M_2 internal tide may refract because of the β effect. As shown in Eq. (2), the propagation speed of internal tides is a function of latitude (note that $f \equiv 2\Omega\sin(\text{latitude})$, where Ω is the rotation rate of the Earth). The latitudinal dependence of the propagation speed is shown in Fig. 9a. It shows that the eigenvalue speed C_n (without rotation) does not change much with latitude in the Tasman Sea (50°–35°S). However, the phase speed C_p (with rotation) decreases monotonically toward the equator in this latitudinal range (black line). It is expected that internal tides refract toward the equator (lower phase speed) when their propagation directions have an angle with the spatial gradients of phase speed (Rainville and Pinkel 2006; Eden and Olbers 2014).

This theoretical prediction is verified in this study by the M_2 internal tide field from satellite altimetry. The

propagation directions (i.e., the directions of the plane wave fitted waves) of the three internal tidal beams are shown in Figs. 9b–d (gray). Although these curves have significant spatial variations as a result of the irregular distribution of altimeter data (section 2c), one can see obvious trends on the central and northern beams. To highlight these trends, we superimpose on the raw curves their second-order polynomial fits (black lines). The results show that the central beam bends toward the equator from 155° to 140° (Fig. 9b) and the northern beam from 145° to 130° (Fig. 9d). The southern beam does not refract much (Fig. 9c) because it occupies a small latitudinal range (53°–51°S) over which the speed does not change much (Fig. 9a).

The refraction of the M_2 internal tide occurs because its propagation speed changes with the latitudinal variation of f, that is, the β effect (Fig. 9a). In a previous study, the refraction of the O_1 and K_1 internal tides has been observed in the South China Sea and the western Pacific (Zhao 2014). In addition, the topographic refraction of the M_2 internal tide is also observed in the Tasman Sea (Klymak et al. 2016). It is worthy to note that previous studies also revealed that internal tides may refract because of the influence of eddies (e.g., Rainville and Pinkel 2006; Park and Farmer 2013; Zaron and Egbert 2014).

e. Convergence and divergence

Another notable feature is the convergence and divergence of the central internal tidal beam. To demonstrate this feature, we show the iso-phase contours of 310° (Greenwich phase) along this beam (Fig. 10, green curves). From the Macquarie Ridge to the Tasman slope, there are nine wave fronts (labeled as W1–W9), whose spatial intervals are one wavelength about 180 km. The results indicate that it takes the M_2 internal tide about eight cycles (≈4 days) to travel across the Tasman Sea. In particular, the wave fronts switch from concave (W1–W3) to convex (W6–W8) with propagation. In its source region, the initial wave fronts are concave, which are determined by the shape of the local submarine ridge. As a result, the beam converges around 155.5°E, 45.5°S and diverges beyond the focal region. This feature is similar to the westward internal tide radiation from the Mariana Arc (Zhao and D'Asaro 2011). The Mariana Arc is about 2000 km long so that it makes a perfect focal region. In contrast, the source submarine ridge in this case is only 500 km long (compared to a wavelength of 180 km); therefore, the resultant focal region here is blurred.

One intriguing feature needs further scrutiny: Why do the internal tide and Macquarie Ridge have an angle in the source region (see W1 in Fig. 10)? Assuming the internal

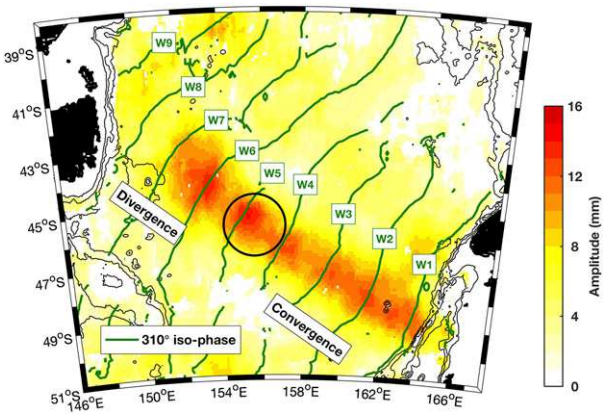

FIG. 10. Convergence and divergence of the central M_2 beam in the Tasman Sea. Color shading indicates the amplitude of the northwestward M_2 internal tide. Green lines W1–W9 indicate the iso-phase contours of Greenwich phase 310°. The wave fronts switch from concave to convex, suggesting that the central beam first converges and then diverges, with a focal region around 155.5°E, 45.5°S.

tide is generated synchronously along the Macquarie Ridge, we would expect that the resultant internal tide wave front is parallel to the ridge. This inconsistency motivates us to examine the geometry of the Macquarie Ridge, the surface tide, and the internal tide. Figure 11a shows the chart of the volume transport ($m^3 s^{-1}$) of the M_2 surface tide around New Zealand from the tide model TPXO8 (Egbert and Erofeeva 2002). Amplitude and phase are shown by colors and lines, respectively. It shows that the M_2 surface tide rotates counterclockwise around New Zealand. This feature has long been reported by New Zealand oceanographers (e.g., Heath 1984; Walters et al. 2001; Chiswell et al. 2015). One can clearly see that the iso-phase contours of the M_2 surface tide have an angle with the Macquarie Ridge (Fig. 11b). The phase on the northern section leads by about 40°. According to the Huygens–Fresnel principle, the outgoing internal tide has an angle with the Macquarie Ridge, with its northern section leading the southern section. According to the 40° phase lag and 180-km wavelength, the northern section is about 20 km farther away from the ridge. Therefore, the propagation direction of internal tides is not perpendicular to the source ridge.

f. Reflection on the Tasman continental slope

One motivating question of the TTIDE/T-Beam/T-Shelf field experiment is how the incident internal tide evolves on the Tasmanian slope (Pinkel et al. 2015). In theory, it is expected that a fraction of the M_2 internal tide reflects back into the open ocean because the Tasmanian continental slope is supercritical to M_2. The

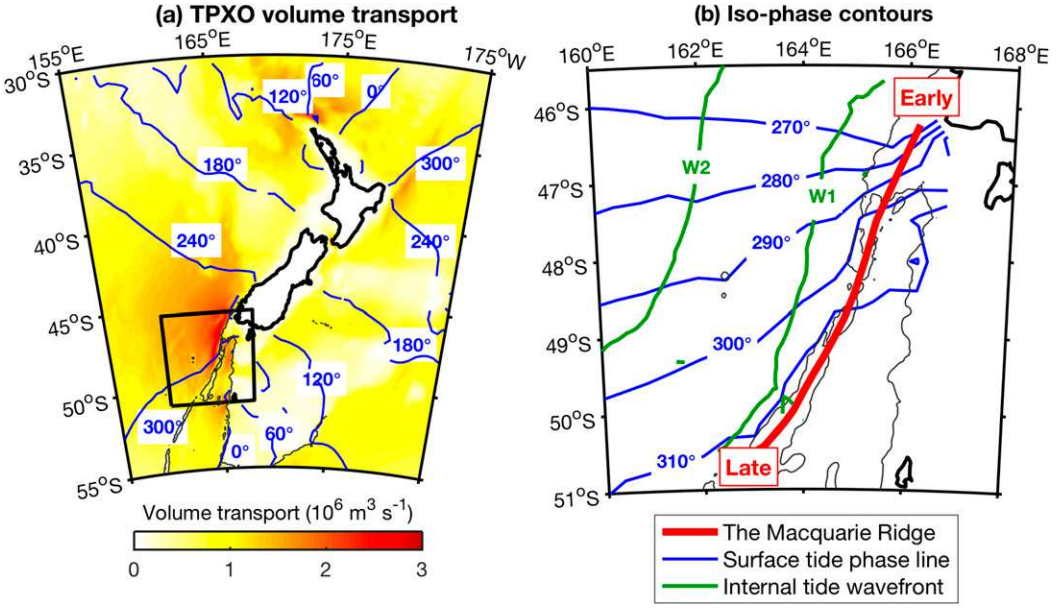

FIG. 11. (a) Amplitude and phase of the volume transport of the M_2 surface tide around New Zealand, predicted from TPXO8. Colors indicate the amplitude. Blue lines indicate iso-phase lines, labeled with the Greenwich phases. Black lines indicate bathymetric contours of 2000-m depth. (b) Geometry of the Macquarie Ridge, the surface tide, and the internal tide. The surface tide (blue) and the Macquarie Ridge (red) have an angle. The surface tide at the northern section of the ridge leads that at the southern section by about 40°. According to the Huygens–Fresnel principle, the generated internal tide has an angle with the Macquarie Ridge, with its northern section leading by 40° or 20 km.

internal tide reflection has been observed by gliders (Johnston et al. 2015) and simulated using numerical models (Klymak et al. 2016). Here, we investigate the incident and reflected M_2 internal tides by satellite altimetry. We have fit three M_2 internal tidal waves of arbitrary propagation directions at each grid point (section 3a). We separate the incident and reflected internal tides by their propagation directions. Here, the incident internal tide is obtained by choosing waves with direction ranging 90°–200° (Fig. 12a) and the reflected internal tide ranging 30°–90° (Fig. 12b). The separation benefits from our three-wave decomposed internal tide field by the plane wave fit method (Fig. 3).

Figure 12 shows that the transbasin M_2 internal tide hits the Tasmanian slope at an angle (Fig. 12a) and reflects back into the open ocean (Fig. 12b). In particular, we can see two outstanding reflected internal tidal beams (blue arrows). Here, we examine whether the incident and reflected waves abide by Snell's law. The reflection wall is represented by the 2000-m isobathic contour and is approximated by a straight line. The approximation of the slope as a wall is appropriate for reflection of mode-1 internal tides, given the small lateral extent of the continental slope relative to one M_2 wavelength. Two black arrows denote the incident internal tide toward the Tasmanian slope, with an incidence angle of 143°. The reflected waves are denoted by two blue arrows toward 31°. In Fig. 12, the incident waves, the reflected waves, and the walls are plotted according to Snell's law. One can see that our altimetric observations agree with the reflection law very well, suggesting that the northeastward internal tidal beams are reflected waves off the Tasmanian slope.

Our altimetric results are consistent with numerical simulations using realistic topography by Klymak et al. (2016), who showed that the incoming internal tidal beam bifurcates because of topographic diffraction of the east Tasman Plateau (see their Fig. 9). As a result, there are two internal tidal beams incident on the slope and correspondingly two reflected beams. The incident and reflected beams from altimetry and those from numerical modeling agree well in location, further confirming our above interpretation.

Reflectivity, or how much incident internal tide reflects on a slope, is a key parameter in quantifying the fate of the M_2 internal tide in the global ocean (Kelly et al. 2013; Johnston et al. 2015). Using glider measurements, Johnston et al. (2015) reported that the reflectivity of the M_2 internal tide ranges 70%–100% on the Tasmanian slope. Using numerical models, Klymak et al. (2016) reported a reflectivity of ≈65%. Here, we estimate the reflectivity from the incident and reflected

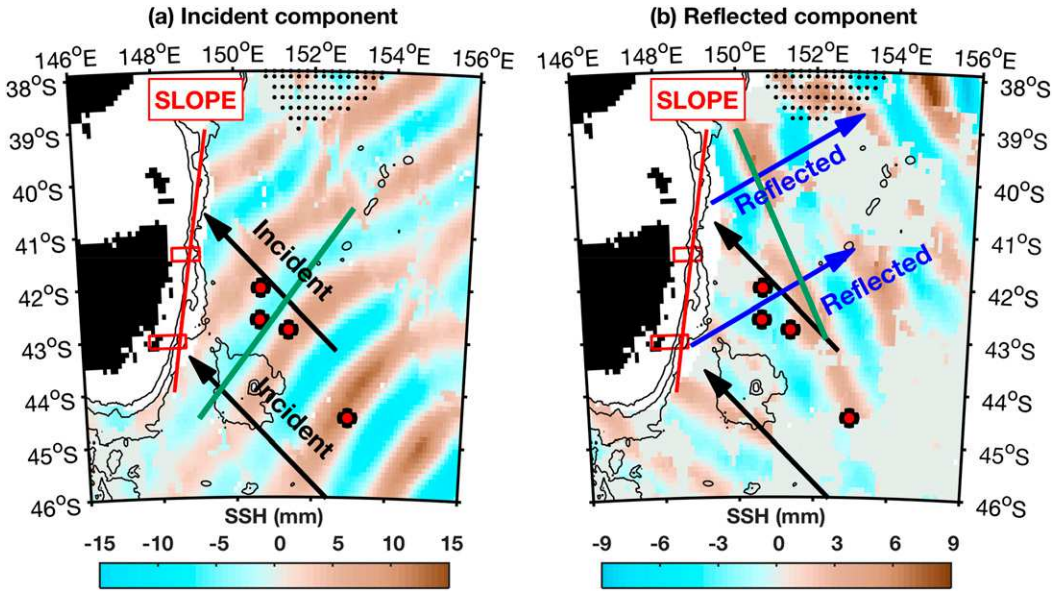

FIG. 12. Reflection of the M_2 internal tide on the Tasmanian slope. (a) Incident component (ranging 90°–200°). (b) Reflected component (ranging 30°–90°). The red line denotes on the Tasmanian slope (the wall), obtained by linear fitting the 2000-m isobathic contour. Black and blue arrows denote the incident and reflected waves, respectively. Two outstanding reflected beams are identified. Their propagation directions abide by Snell's law. Reflectivity is estimated using the incident and reflected energy fluxes across two green lines. Red dots denote four moorings deployed in the 2015 TTIDE/T-Beam/T-Shelf field experiment.

energy fluxes of the M_2 internal tide. The cross beam–integrated fluxes for the incident and reflected internal tides are calculated along the green lines in Fig. 12. To account for the spatial variability, we calculate the integrated fluxes over one wavelength along its propagation direction (±90 km with reference to green lines) and obtain its mean and spatial variability. The incident and reflected fluxes are 0.37 ± 0.07 GW and 0.22 ± 0.04 GW, respectively, yielding a reflectivity of ≈60% on the Tasmanian slope. Our estimation method has large uncertainties caused by several factors. For example, neither the incident nor the reflected energy fluxes contain the time-variable component. In addition, there may be local internal tide generation on the Tasmanian slope. Our estimate is consistent with the values reported by Johnston et al. (2015) and Klymak et al. (2016). The discrepancy is reasonable, considering that 1) the reflectivity on a slope may be a function of space and time, and 2) these three methods have different sampling strategies in space and time. All these studies support the hypothesis that the supercritical Tasmanian slope reflects the M_2 internal tide significantly (Pinkel et al. 2015).

g. *Energetics*

In this section, we examine the depth-integrated energy flux of the M_2 internal tide in the Tasman Sea. We first estimate the total flux from the Macquarie Ridge into the Tasman Sea. In the northwestward internal tide field (Fig. 7d), we integrate the energy fluxes along a section parallel to the ridge (green line). We obtain a total energy flux of 2.2 GW (1 GW = 10^9 W). Likewise, we estimate the energy flux for each of these three beams (divided by green dots). The energy fluxes for the northern, central, and southern beams are 0.4, 1.1, and 0.7 GW, respectively (Table 1). The dominant central beam contributes about half of the total internal tide radiation. Our estimates are lower bounds because the satellite results represent a 20-yr-long phase-locked internal tide field and lack the time-variable component (Ansong et al. 2015; Buijsman et al. 2017).

We next examine the decay of the central internal tidal beam. We sample the beam from the Macquarie Ridge to the Tasmanian slope using 100 equally spaced sections. At each section we integrate across the beam the energy fluxes perpendicular to the section (Fig. 13a). It shows that the beamwidth is about 400 km and does not change much in the propagation. The cross beam–integrated along-beam flux is given in Fig. 13b. It shows that the beam loses little energy in its first ≈1000-km propagation. There are two likely reasons for this. First, the bottom in this region is flat, as shown in Fig. 1. Bottom roughness, in particular large-amplitude topographic features, significantly scatter mode-1 internal tides (Johnston and

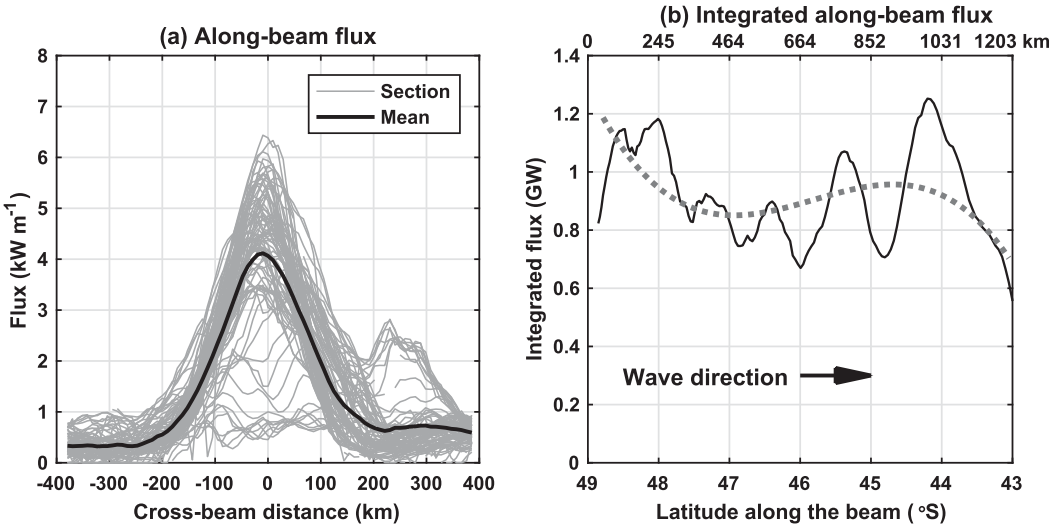

FIG. 13. (a) Along-beam energy flux of the central beam as a function of cross-beam distance. Gray lines denote energy fluxes at 100 evenly sampled sections. (b) Cross beam–integrated along-beam energy flux. Black line denotes the cross beam–integrated energy flux. Dotted line is the second-order polynomial fit.

Merrifield 2003; Bühler and Holmes-Cerfon 2011; Mathur et al. 2014). Second, mesoscale eddies in this region are weak. Previous studies suggest that mesoscale eddies may scatter low-mode internal tides and reduce the coherence of internal tides by time-variable refraction (Zaron and Egbert 2014; Dunphy and Lamb 2014; Dunphy et al. 2017). As shown in Fig. 1, the southern and northwestern parts of the Tasman Sea are affected by the ACC and EAC, respectively, although its eastern and central parts are quiescent. The altimetric flux increases slightly between 47° and 45°S (Fig. 13), likely because of the spatial variation of propagation direction and beamwidth.

4. Summary

In this paper, we constructed the M_2 internal tide field in the Tasman Sea from multisatellite altimeter data using an improved plane wave fit method. We revealed some basic features of the M_2 internal tide in the Tasman Sea. We presented the geographic distribution of the outgoing M_2 internal tide from the Macquarie Ridge. We investigated the transbasin internal tidal beam and revealed its convergence, divergence, refraction, reflection, and energetics. Our two-dimensional view from space provides a spatial context for the TTIDT/T-Beam/T-Shelf field measurements. Our main scientific results are summarized as follows:

1) The Macquarie Ridge radiates three M_2 internal tidal beams into the Tasman Sea (Fig. 7). The southern and northern beams propagate into the ACC and EAC regions, respectively, and become undetectable to satellite altimetry. The central beam propagates over 1500 km across the Tasman Sea and impinges on the Tasmanian continental slope.
2) The propagation speed of the M_2 internal tide is strongly affected by Earth's rotation because the Tasman Sea is at high latitudes. The observed and theoretical propagation speeds agree well (Fig. 8).
3) Both the northern and central beams refract toward the equator by about 15° in propagation because of the β effect (Fig. 9). The propagation speed is a function of latitude, decreasing toward the equator. The change in speed is due to the latitudinal variation of f, that is, the β effect.
4) Because the submarine ridge in the source region has a concave shape, the central internal tidal beam first converges and then diverges in propagation. The focal region is around 155.5°E, 45.5°S (Fig. 10).
5) Two reflected internal tidal beams are observed to propagate northeastward from the Tasmanian slope. The incident beams, the reflected beams, and the slope abide by Snell's law (Fig. 12). We estimate that the reflectivity is about 60%, consistent with previous estimates using glider measurements and numerical modeling.
6) Integrated along the ≈1300-km Macquarie Ridge, the total energy flux into the Tasman Sea is about 2.2 GW. The energy fluxes for the northern, central, and southern beams are 0.4, 1.1, and 0.7 GW, respectively (Table 1).
7) The central beam loses little energy in its first 1000-km propagation (Fig. 13). We suggest two likely reasons

for this slow decay: flat bottom topography and weak mesoscale eddies. In contrast, the beam decays quickly afterward because it encounters rough bottom over the east Tasman Plateau and strong eddies associated with the EAC.

8) Last, but not least, this work suggests the benefits to be gained from regional internal tide studies from satellite altimetry. Careful examination can identify optimizations for the relative orientation of the regional internal tide beams and satellite ground tracks as well as identify unexpected local internal wave dynamics such as reflection, refraction, and focusing.

Acknowledgments. This work was supported by the National Science Foundation via the collaborative TTIDE project (OCE1129246, OCE1129763, and OCE1130048). ZZ was supported by the National Science Foundation (OCE1634041) and the National Aeronautics and Space Administration (NNX17AH57G). We thank Jody Klymak, Sam Kelly, and Amy Waterhouse for comments on an earlier manuscript. This manuscript was greatly improved with suggestions from two anonymous reviewers. We appreciate their time and help. The satellite altimeter products were produced by Ssalto/Duacs and distributed by Archiving, Validation, and Interpretation of Satellite Oceanographic Data (AVISO), with support from CNES (http://www.aviso.altimetry.fr). The *World Ocean Atlas 2013* is produced and made available by NOAA National Oceanographic Data Center (https://www.nodc.noaa.gov/OC5/woa13/). The TPXO tide model is from the Oregon State University (http://volkov.oce.orst.edu/tides/global.html). The internal tide products presented in this paper are available upon request (zzhao@apl.washington.edu).

REFERENCES

Alford, M. H., 2003: Redistribution of energy available for ocean mixing by long-range propagation of internal waves. *Nature*, **423**, 159–162, https://doi.org/10.1038/nature01628.

——, and Z. Zhao, 2007: Global patterns of low-mode internal-wave propagation. Part I: Energy and energy flux. *J. Phys. Oceanogr.*, **37**, 1829–1848, https://doi.org/10.1175/JPO3085.1.

——, J. A. MacKinnon, Z. Zhao, R. Pinkel, J. Klymak, and T. Peacock, 2007: Internal waves across the Pacific. *Geophys. Res. Lett.*, **34**, L24601, https://doi.org/10.1029/2007GL031566.

Ansong, J. K., B. K. Arbic, M. C. Buijsman, J. G. Richman, J. F. Shriver, and A. J. Wallcraft, 2015: Indirect evidence for substantial damping of low-mode internal tides in the open ocean. *J. Geophys. Res. Oceans*, **120**, 6057–6071, https://doi.org/10.1002/2015JC010998.

Arbic, B. K., A. J. Wallcraft, and E. J. Metzger, 2010: Concurrent simulation of the eddying general circulation and tides in a global ocean model. *Ocean Modell.*, **32**, 175–187, https://doi.org/10.1016/j.ocemod.2010.01.007.

AVISO, 2012: DT CorSSH and DT SLA product handbook. AVISO Altimetry Rep. CLS-DOS-NT-08.341, 17 pp., https://www.aviso.altimetry.fr/fileadmin/documents/data/tools/hdbk_dt_corssh_dt_sla.pdf.

Bühler, O., and M. Holmes-Cerfon, 2011: Decay of an internal tide due to random topography in the ocean. *J. Fluid Mech.*, **678**, 271–293, https://doi.org/10.1017/jfm.2011.115.

Buijsman, M. C., and Coauthors, 2014: Three-dimensional double-ridge internal tide resonance in Luzon Strait. *J. Phys. Oceanogr.*, **44**, 850–869, https://doi.org/10.1175/JPO-D-13-024.1.

——, and Coauthors, 2016: Impact of parameterized internal wave drag on the semidiurnal energy balance in a global ocean circulation model. *J. Phys. Oceanogr.*, **46**, 1399–1419, https://doi.org/10.1175/JPO-D-15-0074.1.

——, B. K. Arbic, J. G. Richman, J. F. Shriver, A. J. Wallcraft, and L. Zamudio, 2017: Semidiurnal internal tide incoherence in the equatorial Pacific. *J. Geophys. Res. Oceans*, **122**, 5286–5305, https://doi.org/10.1002/2016JC012590.

Carter, G. S., and Coauthors, 2008: Energetics of M_2 barotropic-to-baroclinic tidal conversion at the Hawaiian Islands. *J. Phys. Oceanogr.*, **38**, 2205–2223, https://doi.org/10.1175/2008JPO3860.1.

Chiswell, S. M., H. C. Bostock, P. J. H. Sutton, and M. J. M. Williams, 2015: Physical oceanography of the deep seas around New Zealand: A review. *N. Z. J. Mar. Freshwater Res.*, **49**, 286–317, https://doi.org/10.1080/00288330.2014.992918.

Dunphy, M., and K. G. Lamb, 2014: Focusing and vertical mode scattering of the first mode internal tide by mesoscale eddy interaction. *J. Geophys. Res. Oceans*, **119**, 523–536, https://doi.org/10.1002/2013JC009293.

——, A. L. Ponte, P. Klein, and S. Le Gentil, 2017: Low-mode internal tide propagation in a turbulent eddy field. *J. Phys. Oceanogr.*, **47**, 649–665, https://doi.org/10.1175/JPO-D-16-0099.1.

Eden, C., and D. Olbers, 2014: An energy compartment model for propagation, nonlinear interaction, and dissipation of internal gravity waves. *J. Phys. Oceanogr.*, **44**, 2093–2106, https://doi.org/10.1175/JPO-D-13-0224.1.

Egbert, G. D., and R. D. Ray, 2000: Significant dissipation of tidal energy in the deep ocean inferred from satellite altimeter data. *Nature*, **405**, 775–778, https://doi.org/10.1038/35015531.

——, and S. Y. Erofeeva, 2002: Efficient inverse modeling of barotropic ocean tides. *J. Atmos. Oceanic Technol.*, **19**, 183–204, https://doi.org/10.1175/1520-0426(2002)019<0183:EIMOBO>2.0.CO;2.

Garrett, C., and E. Kunze, 2007: Internal tide generation in the deep ocean. *Annu. Rev. Fluid Mech.*, **39**, 57–87, https://doi.org/10.1146/annurev.fluid.39.050905.110227.

Gill, A. E., 1982: *Atmosphere–Ocean Dynamics.* Academic Press, 662 pp.

Heath, R. A., 1984: Tidal observations on the West Coast, South Island, New Zealand. *N. Z. J. Mar. Freshwater Res.*, **18**, 251–261, https://doi.org/10.1080/00288330.1984.9516046.

Helfrich, K. R., and R. H. J. Grimshaw, 2008: Nonlinear disintegration of the internal tide. *J. Phys. Oceanogr.*, **38**, 686–701, https://doi.org/10.1175/2007JPO3826.1.

Johnston, T. M. S., and M. A. Merrifield, 2003: Internal tide scattering at seamounts, ridges, and islands. *J. Geophys. Res.*, **108**, 3180, doi:10.1029/2002JC001528.

——, D. L. Rudnick, and S. M. Kelly, 2015: Standing internal tides in the Tasman Sea observed by gliders. *J. Phys. Oceanogr.*, **45**, 2715–2737, https://doi.org/10.1175/JPO-D-15-0038.1.

Kelly, S. M., J. D. Nash, K. I. Martini, M. H. Alford, and E. Kunze, 2012: The cascade of tidal energy from low to high modes on a continental slope. *J. Phys. Oceanogr.*, **42**, 1217–1232, https://doi.org/10.1175/JPO-D-11-0231.1.

——, N. L. Jones, J. D. Nash, and A. F. Waterhouse, 2013: The geography of semidiurnal mode-1 internal-tide energy loss. *Geophys. Res. Lett.*, **40**, 4689–4693, https://doi.org/10.1002/grl.50872.

Kerry, C. G., B. S. Powell, and G. S. Carter, 2013: Effects of remote generation sites on model estimates of M_2 internal tides in the Philippine Sea. *J. Phys. Oceanogr.*, **43**, 187–204, https://doi.org/10.1175/JPO-D-12-081.1.

Klymak, J. M., M. H. Alford, R. Pinkel, R.-C. Lien, Y. J. Yang, and T.-Y. Tang, 2011: The breaking and scattering of the internal tide on a continental slope. *J. Phys. Oceanogr.*, **41**, 926–945, https://doi.org/10.1175/2010JPO4500.1.

——, H. L. Simmons, D. Braznikov, S. Kelly, J. MacKinnon, M. Alford, R. Pinkel, and J. D. Nash, 2016: Reflection of linear internal tides from realistic topography: The Tasman continental slope. *J. Phys. Oceanogr.*, **46**, 3321–3337, https://doi.org/10.1175/JPO-D-16-0061.1.

Kunze, E., 2017a: The internal-wave-driven meridional overturning circulation. *J. Phys. Oceanogr.*, **47**, 2673–2689, https://doi.org/10.1175/JPO-D-16-0142.1.

——, 2017b: Internal-wave-driven mixing: Global geography and budgets. *J. Phys. Oceanogr.*, **47**, 1325–1345, https://doi.org/10.1175/JPO-D-16-0141.1.

——, L. K. Rosenfeld, G. S. Carter, and M. C. Gregg, 2002: Internal waves in Monterey Submarine Canyon. *J. Phys. Oceanogr.*, **32**, 1890–1913, https://doi.org/10.1175/1520-0485(2002)032<1890:IWIMSC>2.0.CO;2.

——, E. Firing, J. M. Hummon, T. K. Chereskin, and A. M. Thurnherr, 2006: Global abyssal mixing inferred from lowered ADCP shear and CTD strain profiles. *J. Phys. Oceanogr.*, **36**, 1553–1576, https://doi.org/10.1175/JPO2926.1.

——, C. MacKay, E. E. McPhee-Shaw, K. Morrice, J. B. Girton, and S. R. Terker, 2012: Turbulent mixing and exchange with interior waters on sloping boundaries. *J. Phys. Oceanogr.*, **42**, 910–927, https://doi.org/10.1175/JPO-D-11-075.1.

Legg, S., and J. Klymak, 2008: Internal hydraulic jumps and overturning generated by tidal flow over a tall steep ridge. *J. Phys. Oceanogr.*, **38**, 1949–1964, https://doi.org/10.1175/2008JPO3777.1.

Locarnini, R. A., and Coauthors, 2013: *Temperature*. Vol. 1, *World Ocean Atlas 2013*, NOAA Atlas NESDIS 73, 40 pp., http://data.nodc.noaa.gov/woa/WOA13/DOC/woa13_vol1.pdf.

MacKinnon, J., L. St. Laurent, and A. N. Garabato, 2013: Diapycnal mixing processes in the ocean interior. *Ocean Circulation and Climate: A 21st Century Perspective*, G. Siedler et al., Eds., International Geophysics Series, Vol. 103, Academic Press, 159–183.

——, and Coauthors, 2017: Climate process team on internal wave–driven ocean mixing. *Bull. Amer. Meteor. Soc.*, **98**, 2429–2454, https://doi.org/10.1175/BAMS-D-16-0030.1.

Martini, K. I., M. H. Alford, E. Kunze, S. M. Kelly, and J. D. Nash, 2013: Internal bores and breaking internal tides on the Oregon continental slope. *J. Phys. Oceanogr.*, **43**, 120–139, https://doi.org/10.1175/JPO-D-12-030.1.

Mathur, M., G. S. Carter, and T. Peacock, 2014: Topographic scattering of the low-mode internal tide in the deep ocean. *J. Geophys. Res. Oceans*, **119**, 2165–2182, https://doi.org/10.1002/2013JC009152.

Melet, A., R. Hallberg, S. Legg, and K. Polzin, 2013: Sensitivity of the ocean state to the vertical distribution of internal-tide-driven mixing. *J. Phys. Oceanogr.*, **43**, 602–615, https://doi.org/10.1175/JPO-D-12-055.1.

——, S. Legg, and R. Hallberg, 2016: Climatic impacts of parameterized local and remote tidal mixing. *J. Climate*, **29**, 3473–3500, https://doi.org/10.1175/JCLI-D-15-0153.1.

Merrifield, M. A., P. E. Holloway, and T. M. S. Johnston, 2001: The generation of internal tides at the Hawaiian Ridge. *Geophys. Res. Lett.*, **28**, 559–562, https://doi.org/10.1029/2000GL011749.

Morozov, E. G., 1995: Semidiurnal internal wave global field. *Deep-Sea Res. I*, **42**, 135–148, https://doi.org/10.1016/0967-0637(95)92886-C.

Müller, M., 2013: On the space- and time-dependence of barotropic-to-baroclinic tidal energy conversion. *Ocean Modell.*, **72**, 242–252, https://doi.org/10.1016/j.ocemod.2013.09.007.

Munk, W. H., B. Zetler, and G. W. Groves, 1965: Tidal cusps. *Geophys. J. Int.*, **10**, 211–219, https://doi.org/10.1111/j.1365-246X.1965.tb03062.x.

——, and C. Wunsch, 1998: Abyssal recipes II: Energetics of tidal and wind mixing. *Deep-Sea Res. I*, **45**, 1977–2010, https://doi.org/10.1016/S0967-0637(98)00070-3.

Nash, J. D., E. Kunze, J. M. Toole, and R. W. Schmitt, 2004: Internal tide reflection and turbulent mixing on the continental slope. *J. Phys. Oceanogr.*, **34**, 1117–1134, https://doi.org/10.1175/1520-0485(2004)034<1117:ITRATM>2.0.CO;2.

Niwa, Y., and T. Hibiya, 2001: Numerical study of the spatial distribution of the M_2 internal tide in the Pacific Ocean. *J. Geophys. Res.*, **106**, 22 441–22 449, https://doi.org/10.1029/2000JC000770.

Park, J.-H., and D. Farmer, 2013: Effects of Kuroshio intrusions on nonlinear internal waves in the South China Sea during winter. *J. Geophys. Res. Oceans*, **118**, 7081–7094, https://doi.org/10.1002/2013JC008983.

Pinkel, R., and Coauthors, 2015: Breaking internal tides keep the ocean in balance. *Eos, Trans. Amer. Geophys. Union*, **96**, https://doi.org/10.1029/2015EO039555.

Ponte, A. L., and B. D. Cornuelle, 2013: Coastal numerical modelling of tides: Sensitivity to domain size and remotely generated internal tide. *Ocean Modell.*, **62**, 17–26, https://doi.org/10.1016/j.ocemod.2012.11.007.

Rainville, L., and R. Pinkel, 2006: Propagation of low-mode internal waves through the ocean. *J. Phys. Oceanogr.*, **36**, 1220–1236, https://doi.org/10.1175/JPO2889.1.

——, T. M. S. Johnston, G. S. Carter, M. A. Merrifield, R. Pinkel, P. F. Worcester, and B. D. Dushaw, 2010: Interference pattern and propagation of the M_2 internal tide south of the Hawaiian Ridge. *J. Phys. Oceanogr.*, **40**, 311–325, https://doi.org/10.1175/2009JPO4256.1.

Ray, R. D., and G. T. Mitchum, 1996: Surface manifestation of internal tides generated near Hawaii. *Geophys. Res. Lett.*, **23**, 2101–2104, https://doi.org/10.1029/96GL02050.

——, and D. E. Cartwright, 2001: Estimates of internal tide energy fluxes from TOPEX/Poseidon altimetry: Central North Pacific. *Geophys. Res. Lett.*, **28**, 1259–1262, https://doi.org/10.1029/2000GL012447.

——, and E. D. Zaron, 2011: Non-stationary internal tides observed with satellite altimetry. *Geophys. Res. Lett.*, **38**, L17609, https://doi.org/10.1029/2011GL048617.

——, and ——, 2016: M_2 internal tides and their observed wavenumber spectra from satellite altimetry. *J. Phys. Oceanogr.*, **46**, 3–22, https://doi.org/10.1175/JPO-D-15-0065.1.

——, G. D. Egbert, and S. Y. Erofeeva, 2011: Tide predictions in shelf and coastal waters: Status and prospects. *Coastal Altimetry*, S. Vignudelli et al., Eds., Springer, 191–216.

Savage, A. C., and Coauthors, 2017: Frequency content of sea surface height variability from internal gravity waves to mesoscale eddies. *J. Geophys. Res. Oceans*, **122**, 2519–2538, https://doi.org/10.1002/2016JC012331.

Simmons, H. L., R. W. Hallberg, and B. K. Arbic, 2004: Internal wave generation in a global baroclinic tide model. *Deep-Sea Res. II*, **51**, 3043–3068, https://doi.org/10.1016/j.dsr2.2004.09.015.

Walters, R. A., D. G. Goring, and R. G. Bell, 2001: Ocean tides around New Zealand. *N. Z. J. Mar. Freshwater Res.*, **35**, 567–579, https://doi.org/10.1080/00288330.2001.9517023.

Waterhouse, A. F., and Coauthors, 2014: Global patterns of diapycnal mixing from measurements of the turbulent dissipation rate. *J. Phys. Oceanogr.*, **44**, 1854–1872, https://doi.org/10.1175/JPO-D-13-0104.1.

——, J. A. MacKinnon, R. C. Musgrave, S. M. Kelly, A. Pickering, and J. Nash, 2017: Internal tide convergence and mixing in a submarine canyon. *J. Phys. Oceanogr.*, **47**, 303–322, https://doi.org/10.1175/JPO-D-16-0073.1.

Waterman, S., A. C. Naveira Garabato, and K. L. Polzin, 2013: Internal waves and turbulence in the Antarctic Circumpolar Current. *J. Phys. Oceanogr.*, **43**, 259–282, https://doi.org/10.1175/JPO-D-11-0194.1.

Wunsch, C., 1975: Internal tides in the ocean. *Rev. Geophys. Space Phys.*, **13**, 167–182, https://doi.org/10.1029/RG013i001p00167.

——, 2013: Baroclinic motions and energetics as measured by altimeters. *J. Atmos. Oceanic Technol.*, **30**, 140–150, https://doi.org/10.1175/JTECH-D-12-00035.1.

——, and R. Ferrari, 2004: Vertical mixing, energy, and the general circulation of the oceans. *Annu. Rev. Fluid Mech.*, **36**, 281–314, https://doi.org/10.1146/annurev.fluid.36.050802.122121.

Zaron, E. D., 2017: Mapping the nonstationary internal tide with satellite altimetry. *J. Geophys. Res. Oceans*, **122**, 539–554, https://doi.org/10.1002/2016JC012487.

——, and G. D. Egbert, 2014: Time-variable refraction of the internal tide at the Hawaiian Ridge. *J. Phys. Oceanogr.*, **44**, 538–557, https://doi.org/10.1175/JPO-D-12-0238.1.

Zhao, Z., 2014: Internal tide radiation from the Luzon Strait. *J. Geophys. Res. Oceans*, **119**, 5434–5448, https://doi.org/10.1002/2014JC010014.

——, 2017: The global mode-1 S2 internal tide. *J. Geophys. Res. Oceans*, **122**, 8794–8812, https://doi.org/10.1002/2017JC013112.

——, and M. H. Alford, 2009: New altimetric estimates of mode-1 M_2 internal tides in the central North Pacific Ocean. *J. Phys. Oceanogr.*, **39**, 1669–1684, https://doi.org/10.1175/2009JPO3922.1.

——, and E. A. D'Asaro, 2011: A perfect focus of the internal tide from the Mariana Arc. *Geophys. Res. Lett.*, **38**, L14609, https://doi.org/10.1029/2011GL047909.

——, M. H. Alford, J. Girton, T. M. S. Johnston, and G. Carter, 2011: Internal tides around the Hawaiian Ridge estimated from multisatellite altimetry. *J. Geophys. Res.*, **116**, C12039, https://doi.org/10.1029/2011JC007045.

——, ——, ——, L. Rainville, and H. L. Simmons, 2016: Global observations of open-ocean mode-1 M_2 internal tides. *J. Phys. Oceanogr.*, **46**, 1657–1684, https://doi.org/10.1175/JPO-D-15-0105.1.

Zweng, M., and Coauthors, 2013: *Salinity*. Vol. 2, *World Ocean Atlas 2013*, NOAA Atlas NESDIS 74, 39 pp., http://data.nodc.noaa.gov/woa/WOA13/DOC/woa13_vol2.pdf.